arXiv:2001.04455v1 [physics.atom-ph] 13 Jan 2020

# High-Fidelity Control, Detection, and Entanglement of Alkaline-Earth Rydberg Atoms

Ivaylo S. Madjarov,[1,*] Jacob P. Covey,[1,*] Adam L. Shaw,[1] Joonhee Choi,[1] Anant Kale,[1] Alexandre Cooper,[1,†] Hannes Pichler,[1] Vladimir Schkolnik,[2] Jason R. Williams,[2] and Manuel Endres[1,‡]
[1] *Division of Physics, Mathematics and Astronomy, California Institute of Technology, Pasadena, CA 91125, USA*
[2] *Jet Propulsion Laboratory, California Institute of Technology, Pasadena, CA 91109, USA*

Trapped neutral atoms have become a prominent platform for quantum science, where entanglement fidelity records have been set using highly-excited Rydberg states. However, controlled two-qubit entanglement generation has so far been limited to alkali species, leaving the exploitation of more complex electronic structures as an open frontier that could lead to improved fidelities and fundamentally different applications such as quantum-enhanced optical clocks. Here we demonstrate a novel approach utilizing the two-valence electron structure of individual alkaline-earth Rydberg atoms. We find fidelities for Rydberg state detection, single-atom Rabi operations, and two-atom entanglement surpassing previously published values. Our results pave the way for novel applications, including programmable quantum metrology and hybrid atom-ion systems, and set the stage for alkaline-earth based quantum computing architectures.

Recent years have seen remarkable advances in generating strong, coherent interactions in arrays of neutral atoms through excitation to Rydberg states, characterized by large electronic orbits [1]. This has led to profound results in quantum science applications, such as quantum simulation [2–4] and quantum computing [5–10], including a record for two-atom entanglement for neutral atoms [8]. Furthermore, up to 20-qubit entangled states have been generated in Rydberg arrays [11], competitive with results in trapped ions [12] and superconducting circuits [13]. Many of these developments were fueled by novel techniques for generating reconfigurable atomic arrays [14–16] and mitigation of noise sources [8, 17]. While previous Rydberg-atom-array experiments have utilized alkali species, atoms with a more complex level structure, such as alkaline-earth atoms (AEAs) [18–24] commonly used in optical lattice clocks [25], provide new opportunities for increasing fidelities and accessing fundamentally different applications, including Rydberg-based quantum metrology [26–28], quantum clock networks [29], and quantum computing schemes with optical and nuclear qubits [30–32].

Here we demonstrate such a novel Rydberg array architecture based on AEAs, where we utilize the two-valence electron structure for single-photon Rydberg excitation from a meta-stable clock state as well as auto-ionization detection of Rydberg atoms [Fig. 1]. We find leading fidelities for Rydberg state detection, coherent operations between ground- and Rydberg-state, and Rydberg-based two-atom entanglement [Table I]. More generally, our results constitute the highest reported two-atom entanglement fidelities for neutral atoms as well as a proof-of-principle for controlled two-atom entanglement between AEAs. We further demonstrate a high-fidelity entanglement operation with optical traps kept on, an important step for gate-based quantum computing [1]. As detailed in the outlook section, our results open up a host of new opportunities for quantum metrology and computing as well as for optical trapping of ions.

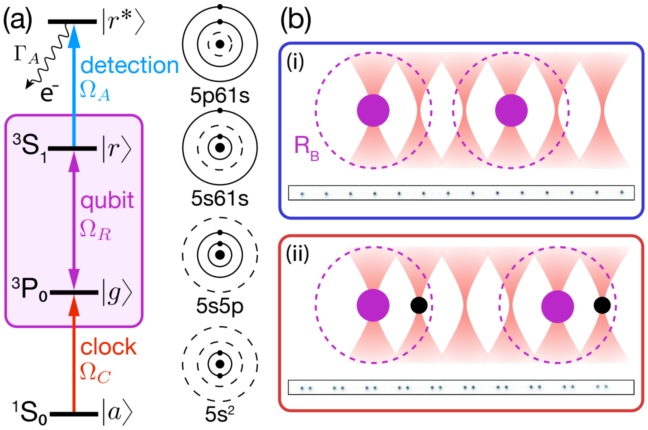

FIG. 1. Schematic. (a) The relevant level structure (left), and electronic configuration (right) for strontium−88. The Rydberg-ground state qubit is defined by a metastable 'clock' state $|g\rangle$ and the 5s61s $^3S_1$ $m_J = 0$ Rydberg state $|r\rangle$ (highlighted with a purple box), which we detect by driving to an auto-ionizing 5p61s state $|r^*\rangle$. The clock state $|g\rangle$ is initialized from the absolute ground state $|a\rangle$. (b) We use atom-by-atom assembly in optical tweezers to prepare an effectively non-interacting configuration [(i), blue box and data-points throughout] and a strongly Rydberg-blockaded pair configuration [(ii), red box and data-points throughout] [4]. The blockade radius $R_B$, where two-atom excitation is suppressed, is indicated by a dashed circle. Throughout, purple and black circles indicate $|r\rangle$ and $|g\rangle$ atoms, respectively. Averaged fluorescence images of atoms in configurations (i) and (ii) are shown.

Our experimental system [23, 33, 34] combines various novel key elements [35]: First, we implement atom-by-atom assembly in reconfigurable tweezer arrays [14, 15] for AEAs [Fig. 1(b)]. Second, we sidestep the typical

---

[*] These authors contributed equally to this work

[†] Permanent address: Institute for Quantum Computing, University of Waterloo, 200 University Ave West, Waterloo, Ontario, Canada

[‡] mendres@caltech.edu

Table I. Uncorrected and SPAM-corrected fidelities for single-atom and Rydberg-blockaded pulses. The ‘T’ indicates settings where the tweezers are on during Rydberg excitation.

| Quantity | Uncorrected | SPAM-corrected |
|---|---|---|
| Single-atom $\pi$-pulse | 0.9951(9) | 0.9967(9) |
| Single-atom $2\pi$-pulse | 0.9951(9) | 0.998(1) |
| Blockaded $\pi$-pulse | 0.992(2) | 0.996(2) |
| Blockaded $2\pi$-pulse | 0.992(2) | 0.999(2) |
| Blockaded $\pi$-pulse, T | 0.992(2) | 0.996(2) |
| Blockaded $2\pi$-pulse, T | 0.987(2) | 0.994(3) |
| Bell state fidelity | $\geq 0.983(2)$ | $\geq 0.995(3)$ |
| Bell state fidelity, T | $\geq 0.978(2)$ | $\geq 0.990(3)$ |

protocol for two-photon excitation to S-series Rydberg states, which requires significantly higher laser power to suppress intermediate state scattering, by transferring atoms to the long-lived $^3\mathrm{P}_0$ clock state $|g\rangle$ [25, 33–36]. We treat $|g\rangle$ as an effective ground state from which we apply single-photon excitation to a $^3\mathrm{S}_1$ Rydberg state $|r\rangle$ [26]. Third, instead of relying on loss through tweezer anti-trapping as in alkali systems, we employ a rapid auto-ionization scheme for Rydberg state detection. In contrast to earlier implementations of auto-ionization detection in bulk gases [37, 38], we image remaining neutral atoms [33] instead of detecting charged particles.

More generally, our findings improve the outlook for Rydberg-based quantum computing [1], optimization [39], and simulation [2–4, 40, 41]. These applications all rely on high fidelities for preparation, detection, single-atom operations, and entanglement generation for which we briefly summarize our results: We obtain a state preparation fidelity of 0.997(1) through a combination of coherent and incoherent transfer [35]. The new auto-ionization scheme markedly improves the Rydberg state detection fidelity to $0.9963 - 0.9996$ [8, 11]. We also push the limits of single and two-qubit operations in ground-to Rydberg-state transitions [3, 8, 9, 11]. For example, we find $\pi$-pulse fidelities of 0.9951(9) without correcting for state preparation and measurement (SPAM) and 0.9967(9) if SPAM correction is applied [35]. Finally, using a conservative lower-bound procedure, we observe a two-qubit entangled Bell state fidelity of $\geq 0.983(2)$ and $\geq 0.995(3)$ without and with SPAM correction, respectively. We note that all values are obtained on average and for parallel operation in arrays of 14 atoms or 10 pairs for the non-interacting or pair-interacting case, respectively.

We begin by analyzing short-time Rabi oscillations between $|g\rangle$ and $|r\rangle$ [Fig. 2(a)] and the auto-ionization detection scheme [Fig. 2(b)] in an essentially non-interacting atomic configuration [(i) in Fig. 1(b)]. To detect atoms in $|r\rangle$ we excite the core valence-electron from a 5s to a 5p level [35], which then rapidly auto-ionizes the Rydberg electron [inset of Fig. 2(b)]. The ionized atoms are dark to subsequent detection of atoms in $|g\rangle$ [33], providing the means to distinguish ground and Rydberg atoms.

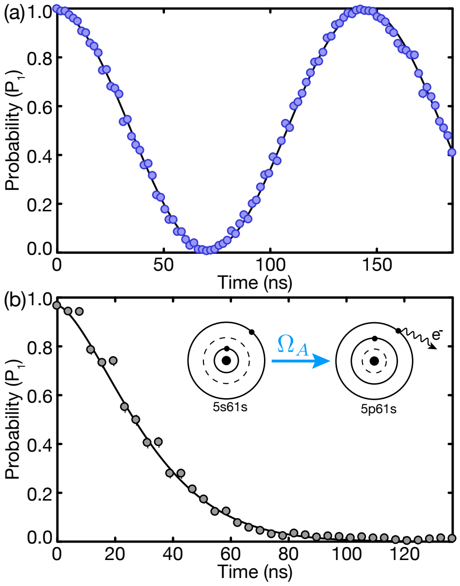

FIG. 2. Rabi oscillations and auto-ionization. (a) Array-averaged probability, $P_1$, of detecting an atom after a resonant Rydberg pulse and subsequent auto-ionization as a function of Rydberg pulse time, showing high-contrast Rabi oscillations with frequency $\Omega_R = 2\pi \times 6.80(2)$ MHz. The auto-ionization pulse time is fixed to 5 $\mu$s. The points are uncorrected data. (b) $P_1$ as a function of auto-ionization pulse time at a fixed Rydberg pulse time of 70 ns corresponding to a $\pi$-pulse (followed by a second $\pi$-pulse). Inset: illustration of the auto-ionization process.

We use a $|g\rangle \leftrightarrow |r\rangle$ Rabi frequency of $\Omega_R \approx 2\pi \times 6 - 7$ MHz throughout, and observe Rabi oscillations with high contrast at a fixed auto-ionization pulse length [Fig. 2(a), Table I]. To quantify the auto-ionization detection, we perform a $\pi$-pulse on $|g\rangle \leftrightarrow |r\rangle$, then apply an auto-ionization pulse for a variable duration [Fig. 2(b)], and then perform a second $\pi$-pulse on $|g\rangle \leftrightarrow |r\rangle$ before measurement. The detected population decreases to zero with a $1/e$ time of $\tau_A = 35(1)$ ns [35]. We can compare $\tau_A$ to the lifetime of $|r\rangle$, which is estimated to be $\tau_{|r\rangle} \approx 80$ $\mu$s [42], placing an upper bound on the $|r\rangle$-state detection efficiency of 0.9996(1). A lower bound comes from the measured $\pi$-pulse fidelity of 0.9963(9) corrected for preparation and ground state detection errors [35]. These limits can be increased with higher laser power and faster switching [35].

To probe our longer-time coherence, we drive the Rydberg transition for as long as 7 $\mu$s [Fig. 3(a)]. The decay of the contrast on longer timescales is well modeled by a Gaussian profile of the form $\mathcal{C}(t) = \mathcal{C}_0 \exp(-t^2/\tau_C^2)$. We find that $\tau_C \approx 7$ $\mu$s is consistent with our data, and corresponds to a $1/e$ coherence of $\approx 42$ cycles. To our knowledge, this is largest number of coherent ground-to-Rydberg cycles that has been published to date [8, 10]. Limitations to short- and long-term coherence are dis-

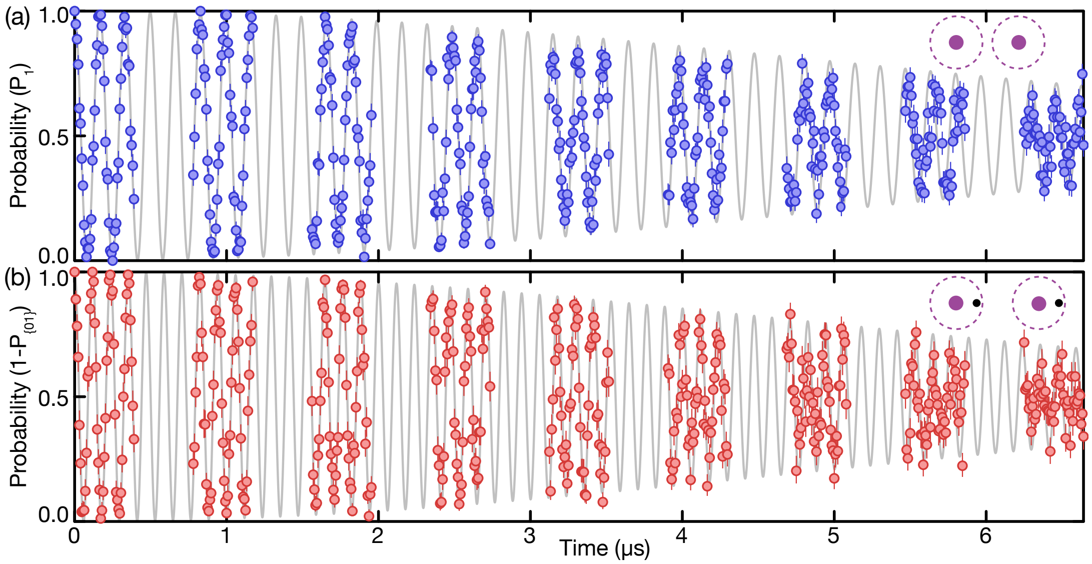

FIG. 3. Long-time Rabi oscillations for single and blockaded atoms. (a) Array-averaged Rabi oscillations for the non-interacting configuration (i), depicted by the inset. We operate with $\Omega_R = 2\pi \times 6.0$ MHz. By fitting with a Gaussian profile, we find a $1/e$ coherence of $\approx 42$ cycles. (b) Same as in (a) but for the blockaded configuration (ii), depicted by the inset. We plot $1 - P_{\{01\}}$, where $P_{\{01\}}$ is the array-averaged symmetrized probability [35] of detecting one atom of an initial pair (and not both). We observe a blockade-enhanced Rabi frequency of $\tilde{\Omega}_R = 2\pi \times 8.5$ MHz. We find a $1/e$ coherence of $\approx 60$ cycles. The points are uncorrected data.

cussed and modeled in detail in Ref. [35]. The main contributing factors are laser intensity and phase noise (which both can be improved upon with technical upgrades, such as cavity filtering of phase noise [8]), and finite Rydberg state lifetime.

We now turn to the pair-interacting configuration [(ii) in Fig. 1(b)] to study blockaded Rabi oscillations [1, 8]. For an array spacing of 3.6 $\mu$m, we anticipate an interaction shift of $V_B \approx 2\pi \times 130$ MHz for the $n = 61$ Rydberg state in the $^3$S$_1$ series [42]. In this configuration, simultaneous Rydberg excitation of closely-spaced neighbors is strongly suppressed, and an oscillation between $|g\rangle$ and the entangled $W$-Bell-state $|W\rangle = (|gr\rangle + e^{i\phi}|rg\rangle)/\sqrt{2}$ is predicted with a Rabi frequency enhanced by a factor of $\sqrt{2}$ [1], as observed in our data. We show our results for long-term coherent oscillations in Fig. 3(b) and find a $1/e$ coherence time corresponding to $\approx 60$ cycles. Results for short-term oscillations are shown in Fig. 4(a) and the fidelity values are summarized in Table I.

We provide a lower bound for the Bell state fidelity based on measured populations at the (blockaded) $\pi$-time and a lower bound on the purity $P$ of the two-atom state [35]. The latter is obtained by measuring the atomic populations at the (blockaded) $2\pi$ time, under the assumption that the purity does not increase between the $\pi$ and the $2\pi$ time. For a detailed discussion and analysis of this bound and the validity of the underlying assumptions, see Ref. [35]. With this approach, we find uncorrected and SPAM-corrected lower bounds on the Bell state fidelity of 0.983(2) and 0.995(3), respectively [Table I].

We note that all preceding results were obtained with the tweezers switched *off* during Rydberg excitation. The potential application of Rydberg gates to large circuit depth quantum computers motivates the study of blockade oscillations with the tweezers *on*. In particular, we foresee challenges for sequential gate-based platforms if tweezers must be turned off during each operation. In general, the prospects for quickly turning off individual tweezers while not perturbing the other atoms in the array are unclear, especially in two dimensions. In systems implementing gates between the absolute ground and clock states for example, blinking traps on and off will eventually lead to heating and loss, ultimately limiting the number of possible operations. To remedy this problem, repulsive traps such as interferometrically-generated bottles [43] or repulsive lattices [9] have been used in lieu of standard optical tweezer arrays [14, 15].

Despite finding that our Rydberg state is anti-trapped (with a magnitude roughly equal to that of the ground state trapping) at our clock-magic wavelength of $\lambda_T = 813.4$ nm [35], we observe high-fidelity entanglement even when the tweezers remain on during Rydberg interrogation. Certain factors make this situation favorable for alkaline-earth atoms. One is the ability to reach lower temperatures using narrow-line cooling, which suppresses thermal dephasing due to trap light shifts. Furthermore, a lower temperature allows for ramping down of tweezers to shallower depths before atoms are lost, further alleviating dephasing. Finally, access to higher Rabi frequencies provides faster and less light-shift-sensitive entangling operations.

We study short-time blockaded Rabi oscillations both with the tweezers switched *off* [Fig. 4(a)] and left *on* [Fig. 4(b)]. We find similar fidelities for the $\pi$- and $2\pi$-pulses in both cases [Table I]. Further, we estimate a

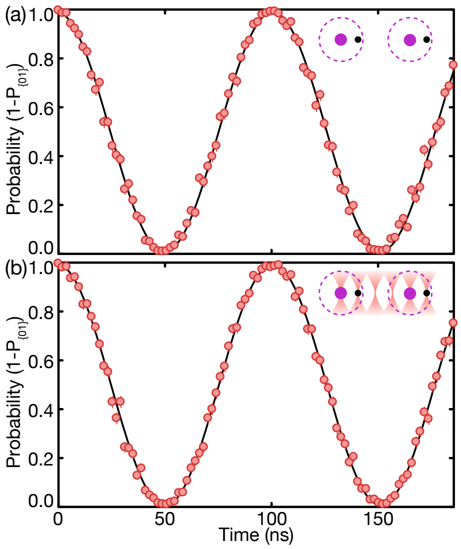

FIG. 4. Short-time Rydberg-blockaded Rabi oscillations with tweezers *off* and *on*. (a) Short-time Rabi-oscillations for the blockade configuration (ii) with the traps *off*, depicted by the inset. (b) Same as in (a) but with tweezers *on* during Rydberg interrogation with a $|g\rangle$-state depth of U/$h \approx 0.94$ MHz. The points are uncorrected data, and the blockade-enhanced Rabi frequency is $\tilde{\Omega}_R = 2\pi \times 9.8$ MHz.

lower bound for the Bell state fidelity in the tweezer *on* case, and find uncorrected and corrected values of $\geq 0.978(2)$ and $\geq 0.990(3)$, respectively. We expect further improvements in shorter-wavelength tweezers for which the Rydberg states of AEAs are trapped [44], and our observations show promise for Rydberg-based quantum computing in a standard tweezer array [14, 15].

Our work bridges the gap between the fields of Rydberg atom arrays and optical clocks [25], opening the door to Rydberg-based quantum-enhanced metrology [26, 27], including the programmable generation of spin-squeezed states [28] in recently demonstrated tweezer clocks [34, 36], and quantum clock networks [29]. Further, the demonstrated entangling operations provide a mechanism for two-qubit gates in AEA-based quantum computation and simulation architectures leveraging optical and nuclear qubits [30–32]. More generally, the observed entanglement fidelities could enable gate fidelities for long-lived ground states approaching fault-tolerant error correction thresholds [45]. In addition, the high Rydberg- and ground-state detection-fidelities could play an important role in applications based on sampling from bit-string probability distributions [39, 46]. Finally, by auto-ionizing the Rydberg electron with high fidelity and noting that we expect the remaining ion to stay trapped, we have found a potential new approach to the optical trapping of ions [47, 48] in up to three dimensional arrays [16, 49]. Such a platform has been proposed as a route to ion-based quantum computing [50] as well as for hybrid atom-ion systems [51–53].

We acknowledge discussions with Chris Greene and Harry Levine as well as funding provided by the Institute for Quantum Information and Matter, an NSF Physics Frontiers Center (NSF Grant PHY-1733907), the NSF CAREER award (1753386), the AFOSR YIP (FA9550-19-1-0044), the Sloan Foundation, and Fred Blum. Research was carried out at the Jet Propulsion Laboratory and the California Institute of Technology under a contract with the National Aeronautics and Space Administration and funded through the Presidents and Directors Research and Development Fund (PDRDF). JPC acknowledges support from the PMA Prize postdoctoral fellowship, and JC acknowledges support from the IQIM postdoctoral fellowship. HP acknowleges support by the Gordon and Betty Moore Foundation. AK acknowledges funding from the Larson SURF fellowship, Caltech Student-Faculty Programs.

*Note added.*—Recently, we became aware of work in ytterbium tweezer arrays demonstrating trapping of Rydberg states [54].

# Supplementary Materials

## APPENDIX A: Summary of experiment

We briefly summarize the relevant features of our $^{88}$Sr experiment [23, 33, 34]. We employ a one-dimensional array of 43 tweezers spaced by 3.6 $\mu$m. Atoms are cooled close to the tranverse motional ground state using narrow line cooling [33, 34, 36], with an average occupation number of $\bar{n}_r \approx 0.3$ ($T_r \approx 2.5$ $\mu$K), in tweezers of ground-state depth $\mathrm{U}_0 \approx k_B \times 450$ $\mu$K $\approx h \times 9.4$ MHz with a radial trapping frequency of $\omega_r \approx 2\pi \times 78$ kHz.

For state preparation [Fig. 1(a)], we drive from the 5s$^2$ $^1$S$_0$ absolute ground state (labeled $|a\rangle$) to the 5s5p $^3$P$_0$ clock state (labeled $|g\rangle$) with a narrow-line laser [34], reaching Rabi frequencies of $\Omega_C \approx 2\pi \times 3.5$ kHz in a magnetic field of $\approx 710$ G [55, 56] (otherwise set to $\approx 71$ G for the entire experiment). We populate $|g\rangle$ with a $\pi$-pulse reaching a loss-corrected fidelity of 0.986(2), which we supplement with incoherent pumping (after adiabatically ramping down the tweezer depth to $\mathrm{U_F} = \mathrm{U}_0/10$) to obtain a clock state population without and with loss correction of 0.997(1) and 0.998(1), respectively. This value is similar to, or higher than, the state preparation fidelities achieved with alkali atoms [9–11, 57].

We treat the long-lived state $|g\rangle$ as a new ground state, from which we drive to the 5s61s $^3$S$_1$, $m_J = 0$ Rydberg state (labeled $|r\rangle$). The $|g\rangle \leftrightarrow |r\rangle$ Rydberg transition occurs at a wavelength of $\lambda_R = 316.7$ nm and we use a $1/e^2$ beam radius of 18(1) $\mu$m. We readily achieve a $|g\rangle \leftrightarrow |r\rangle$ Rabi frequency of $\Omega_R \approx 2\pi \times 6 - 7$ MHz, corresponding to $\approx 30$ mW, and up to $\Omega_R \approx 2\pi \times 13$ MHz with full optimization of the laser system and beam path. To detect atoms in $|r\rangle$ we drive the strong transition to $5p_{3/2}61s_{1/2}$ ($J = 1, m_J = \pm 1$), labelled $|r^*\rangle$. This transition excites the core ion, which then rapidly auto-ionizes the Rydberg electron. The ionized atoms are dark to subsequent detection of atoms in $|g\rangle$ with the high-fidelity scheme described in Ref. [33], providing the means to distinguish ground and Rydberg atoms. We switch off the ramped-down tweezers during the Rydberg pulse [3, 4], after which we apply an auto-ionization pulse while rapidly increasing the depth back to $U_0$ for subsequent read-out.

The Rydberg and clock laser beams are linearly polarized along the magnetic field axis, and the auto-ionization beam is linearly polarized perpendicular to the magnetic field axis. Accordingly, we excite to auto-ionizing states with $m_J = \pm 1$. The tweezers are linearly polarized along the axis of propagation of the Rydberg, clock, and auto-ionization beams – perpendicular to the magnetic field axis.

## APPENDIX B: State preparation

The ground state $|g\rangle$ of our Rydberg qubit is the 5s5p $^3P_0$ metastable clock state of $^{88}$Sr. We populate this state in two stages: first, most atoms are transferred via a coherent $\pi$-pulse on the clock transition. Thereafter, any remaining population is transferred via incoherent pumping.

In our regime where the Rabi frequency of the clock transition ($\Omega_C \approx 2\pi \times 3.5$ kHz) is significantly smaller than the trapping frequency ($\omega_r \approx 2\pi \times 78$ kHz), coherent driving is preferable to incoherent pumping because it preserves the motional state of an atom, i.e., it does not cause heating. However, atomic temperature, trap frequency, trap depth, and beam alignment contribute to the transfer infidelity of coherent driving. Although we drive the clock transition on the motional carrier in the sideband resolved regime, thermal dephasing still plays an important role. Particularly, each motional state has a distinct Rabi frequency, a thermal ensemble of which leads to dephasing [34]. This thermal dephasing is less severe at higher trapping frequencies; however, this can only be achieved in our system by using deeper traps, which would also eventually limit transfer fidelity because of higher rates of Raman scattering out of the clock state. We therefore perform coherent transfer initially in deeper traps ($\approx 450$ $\mu$K), followed immediately by an adiabatic rampdown to one-tenth of that depth. Finally, precise alignment of the clock beam to the tight, transverse axis of the tweezer is important to ensure that no coupling exists to axial motion, which has a much lower trap frequency and thus suffers more thermal dephasing than the transverse direction.

The remaining population is transferred by simultaneous, incoherent driving of the 5s$^2$ $^1S_0 \leftrightarrow$ 5s5p $^3P_1$, 5s5p $^3P_1 \leftrightarrow$ 5s6s $^3S_1$, and 5s5p $^3P_2 \leftrightarrow$ 5s6s $^3S_1$ transitions for 1 ms. This pumping scheme has the clock state as a unique dark state via the decay of 5s6s $^3S_1$ to the clock state and is in general more robust than coherent driving. However, due to photon recoil, differential trapping, and an unfavorable branching ratio of 5s6s $^3S_1$ to the clock state (requiring many absorption and emission cycles), this process causes significant heating, making it unfavorable as compared to coherent driving. Therefore, we only use this method as a secondary step to transfer atoms left behind by the coherent drive.

We measure the fidelity of our state transfer by applying a 750 $\mu$s pulse of intense light resonant with the $^1S_0 \leftrightarrow$ $^1P_1$ transition immediately after state transfer. The large recoil force of this pulse rapidly pushes out atoms in $^1S_0$ with a fidelity of $> 0.9999$ while leaving atoms in the clock state intact. Upon repumping the clock state back into our imaging cycle and imaging the remaining atoms, we obtain a measure of the fraction of atoms that were successfully transferred to the clock state. With coherent driving alone, we measure a state transfer fidelity of 0.986(2), while adding incoherent pumping increases this value to 0.998(1). Both of these values are corrected for loss to quantify state transfer in isolation; however, loss also contributes to infidelity of the overall state *preparation.* Taking loss into account, our overall state preparation fidelity with both coherent driving and incoherent pumping is $\mathcal{F}^{SP} = 0.997(1)$.

## APPENDIX C: Auto-ionization and Rydberg state detection fidelity

The auto-ionization beam is resonant with the Sr$^+$ ionic transition $^2S_{1/2} \leftrightarrow$ $^2P_{3/2}$ at $\lambda_A = 407.6$ nm. The $1/e^2$ beam waist radius is $w_o^A = 16(1)$ $\mu$m with power $P_A = 2.8(4)$ mW, from which we estimate a Rabi frequency of $\Omega_A \approx 2\pi \times 3$ GHz.

To quantify the Rydberg state detection fidelity of our auto-ionization scheme, we compare the observed auto-ionization loss $1/e$ timescale of $\tau_A = 35(1)$ ns to the expected lifetime of $|r\rangle$, which is $\tau_{|r\rangle} \approx 80$ $\mu$s [42]. That is, we compute the probability that an atom in the Rydberg state is auto-ionized before it decays away from the Rydberg state. This estimate places an upper bound on the detection fidelity of $|r\rangle$ to be 0.9996(1), where the uncertainty is dominated by an assumed uncertainty of $\pm 20$ $\mu$s in $\tau_{|r\rangle}$. Note that when the auto-ionization pulse is not applied, there is still a residual detection fidelity of $|r\rangle$ of 0.873(4) due to anti-trapping of $|r\rangle$ in the tweezer (this value is smaller than the previously reported $< 0.98$ for alkalis in part because the atoms are colder here than in previous work [8]). A lower bound on our detection fidelity is given by the measured $\pi$-pulse fidelity after correcting for errors in preparation and ground state detection, which gives 0.9963(9).

Although the auto-ionization rate of $|r^*\rangle$ is $\Gamma_A \sim 100$'s of GHz [37, 38] and we drive the ion core transition with a Rabi frequency $\Omega_A \approx 2\pi \times 3$ GHz, the $|r\rangle \leftrightarrow |r^*\rangle$ transition is inhibited by the continuous quantum Zeno mechanism [58, 59]. Accordingly, the effective auto-ionization rate of $|r\rangle$ is given by $\Gamma_A^{\text{eff}} \approx \Omega_A^2/\Gamma_A$. This is in qualitative agreement with the fact that our measured auto-ionization loss timescale continues to increase with beam intensity, despite the ionic transition being driven far beyond its bare saturation. Furthermore, the finite rise time of the acousto-optic modulator (AOM) that we use for switching the auto-ionization beam is a limiting factor in achieving faster auto-ionization rates. Therefore, detection fidelity can be increased further with higher beam intensity as well as faster beam switching.

## APPENDIX D: State preparation and measurement (SPAM) correction

Our detection basis is binary between zero detected atoms, $\mathbb{0}$, and one detected atom, $\mathbb{1}$, for each site in the array. Two factors affect our ability to correctly determine the occupation of a tweezer: the false positive avoidance probability, $F_0$, and the true positive detection probability, $F_1$. By fitting the bimodal histogram of detected photons for each tweezer and using a binary detection threshold, we determine both $F_0$ and $F_1$, with their errors given by averaging over the whole array [33]. We measure an uncorrected imaging survival probability $S_0$ (with no clock or Rydberg excitation) by measuring how many atoms detected in an image are also detected in a subsequent image. We also measure an uncorrected clock state transfer fidelity $K_0$ by a technique described in Appendix B.

With $F_0$, $F_1$, $S_0$, and $K_0$, we compute a detection-corrected value for survival probability with no clock or Rydberg excitation, $S$, and a detection and survival-corrected value for clock state transfer fidelity, $K$, via

$$S = \frac{S_0 + F_0 - 1}{F_0 + F_1 - 1}, \tag{D1}$$

$$K = \frac{K_0 + F_0 - 1}{S_0 + F_0 - 1}(1 - C). \tag{D2}$$

Here $C = 0.00104(1)$ is the probability of clock state decay before the Rydberg pulse due to Raman scattering from trapping light, estimated by a measure of the lifetime in the clock state at a particular tweezer depth [33] and the time delay between our state preparation and Rydberg interrogation. The total clock state preparation fidelity is then given by $\mathcal{F}^{SP} = KS = 0.997(1)$. While a fraction of the atoms that are unsuccessfully transferred to the clock state end up in the absolute ground state $|a\rangle$, some atoms are instead lost entirely due to heating out of the trap during incoherent pumping. We denote this loss probability by $L$, such that the probability of ending up in $|a\rangle$ is $1 - (K + L)$. Note that we assume all loss captured by $S$ occurs before the start of the Rydberg pulse, while loss during the read-out image that leads to detection infidelity is accounted for by $F_1$.

When considering detection of the Rydberg state, a further detection fidelity, $D$, is introduced which characterizes the fidelity with which an atom that was in the Rydberg state is successfully transferred to a dark ionic state, primarily limited by the finite Rydberg state lifetime. For all calculations we use the theoretical upper bound of $D$, such as to be maximally conservative in our SPAM-correction.

To account for imperfect rearrangement, we post-select our data (both uncorrected and SPAM-corrected) to ac-

Table II. Probabilities entering into SPAM correction calculations.

| Probability | Symbol | Value |
|---|---|---|
| False positive avoidance | $F_0$ | 0.99997(5) |
| Atom detection | $F_1$ | 0.9988(7) |
| Bare survival | $S_0$ | 0.9979(3) |
| Corrected survival | $S$ | 0.9991(7) |
| Bare $\|g\rangle$ transfer | $K_0$ | 0.997(1) |
| Corrected $\|g\rangle$ transfer | $K$ | 0.998(1) |
| Loss during $\|g\rangle$ transfer | $L$ | 0.0008(8) |
| Rydberg state detection | $D$ | 0.9996(1) |

Table III. Populations in the single-atom four-state basis. Note that the sum of these populations equals unity for any $P_r^{'}$, where $P_r^{'}$ is the SPAM-corrected $|r\rangle$ population.

| State | Symbol | Value |
|---|---|---|
| Null (atom lost) | $P_l$ | $1 - S + SL$ |
| $^1$S$_0$ (absolute ground state) | $P_a$ | $S(1 - L - K)$ |
| $^3$P$_0$ (clock) | $P_g$ | $KS(1 - P_r^{'})$ |
| $^3$S$_1$ (Rydberg state) | $P_r$ | $KSP_r^{'}$ |

Table IV. Populations in the two-atom 16-state basis. Note that the sum of these populations equals unity for any pulse fidelities $P_{rg}^{'}$, $P_{gr}^{'}$, and $P_{rr}^{'}$, where $P_{rg}^{'}$ and $P_{gr}^{'}$ are the SPAM-corrected populations of states with one Rydberg excitation, and $P_{rr}^{'}$ is the similarly corrected population of the $P_{rr}$ state. For cases where the initial state $|gg\rangle$ is not properly prepared, the factor of $P_c = P_r^{'}\cos^2(\mathcal{A}/(2\sqrt{2}))$ captures the non-blockaded Rydberg Rabi excitation, where $\mathcal{A}$ is either $\pi$ or $2\pi$. Note that terms expressed in $\{,\}$ are assumed to have a symmetric partner, e.g. $P_{al} \equiv P_{la}$.

| States | Symbol | Value |
|---|---|---|
| (Lost, Lost) | $P_{ll}$ | $(1 - S + SL)^2$ |
| {Lost, $^1$S$_0$} | $P_{la}$ | $(1 - S + SL)S(1 - L - K)$ |
| {Lost, $^3$P$_0$} | $P_{lg}$ | $(1 - S + SL)SK(1 - P_c)$ |
| {Lost, $^3$S$_1$} | $P_{lr}$ | $(1 - S + SL)SKP_c$ |
| ($^1$S$_0$, $^1$S$_0$) | $P_{aa}$ | $S^2(1 - L - K)^2$ |
| {$^1$S$_0$, $^3$P$_0$} | $P_{ag}$ | $S(1 - L - K)SK(1 - P_c)$ |
| {$^1$S$_0$, $^3$S$_1$} | $P_{ar}$ | $S(1 - L - K)SKP_c$ |
| ($^3$P$_0$, $^3$P$_0$) | $P_{gg}$ | $K^2S^2(1 - P_{rg}^{'} - P_{gr}^{'} - P_{rr}^{'})$ |
| ($^3$P$_0$, $^3$S$_1$) | $P_{gr}$ | $K^2S^2P_{gr}^{'}$ |
| ($^3$S$_1$, $^3$P$_0$) | $P_{rg}$ | $K^2S^2P_{rg}^{'}$ |
| ($^3$S$_1$, $^3$S$_1$) | $P_{rr}$ | $K^2S^2P_{rr}^{'}$ |

count only for instances where a target number of atoms (either one atom or two neighboring atoms in the case of blockaded oscillations) have no further neighboring atoms detected within a two-tweezer distance in any of the images following rearrangement. We do not correct for false negative detections of neighboring atoms that may increase infidelity due to interactions. False negatives of such neighbors are rare because of an already small rate of false negative detection, but are even further suppressed by rearrangement and the fact that we use two images to post-select on such events

### 1. Correcting the single-atom pulse fidelities

Having defined the relevant states, their preparation probabilities, and detection fidelities, we now turn to converting the detection basis of $\mathbb{0}$ and $\mathbb{1}$ into the basis of $|g\rangle$ and $|r\rangle$ to perform SPAM-correction. The bare, measured value $P_1$ shown in Figs. 2 and 3 of the main text gives the probability of measuring $\mathbb{1}$ in the detection basis, which corresponds to positively detecting the combined population in $|a\rangle$ and $|g\rangle$ plus the probability of a false positive when no neutral atom is present. This can be quantified by writing $P_1$ in terms of the values in Tables II and III:

$$P_1 = (P_a + P_g + P_r(1-D))F_1 + (P_l + P_r D)(1-F_0). \tag{D3}$$

We put in all the quantities from Table III and solve for $P_r^{'}$, the desired quantity, to obtain:

$$P_r^{'} = \frac{SF_1 + (1-S)(1-F_0) - LS(F_0+F_1-1) - P_1}{KSD(F_0+F_1-1)}. \tag{D4}$$

For the single-atom short-time Rabi oscillations shown in Fig. 2 of the main text, we observe the bare values of $P_1(\pi) = 0.0049(9)$ and $P_1(2\pi) = 0.9951(9)$, yielding pulse fidelities of $\mathcal{F}^{\mathrm{SPAM}}(\pi) = P_r^{'}(\pi) = 0.9967(9)$ and $\mathcal{F}^{\mathrm{SPAM}}(2\pi) = 1 - P_r^{'}(2\pi) = 0.998(1)$, respectively.

### 2. Correcting the two-atom pulse fidelities

For the atomic configuration (ii), there are 16 possible states for each atom pair. Similarly to Table III, we can write populations of each of these states in terms of the survival and transfer fidelities in Table II, as shown in Table IV.

We now write the experimentally measured quantities $P_{10}, P_{00}$, and $P_{11}$ in terms of the values in Tables II and IV. For notational simplicity we define $\bar{F}_0 \equiv (1-F_0)$, and similarly for $F_1$ and $D$:

$$\begin{aligned}
P_{10} = {} & P_{ll}(\bar{F}_0 F_0) \\
& + P_{la}(\bar{F}_0 \bar{F}_1) \\
& + P_{al}(F_1 F_0) \\
& + P_{lg}(\bar{F}_0 \bar{F}_1) \\
& + P_{gl}(F_1 F_0) \\
& + P_{lr}(\bar{F}_0 F_0 D + \bar{F}_0 \bar{D} \bar{F}_1) \\
& + P_{rl}(\bar{F}_0 D F_0 + F_1 \bar{D} F_0) \\
& + P_{aa}(F_1 \bar{F}_1) \\
& + P_{ag}(F_1 \bar{F}_1) \\
& + P_{ga}(F_1 \bar{F}_1) \\
& + P_{ar}(F_1 D F_0 + F_1 \bar{D} \bar{F}_1) \\
& + P_{ra}(F_1 \bar{D} \bar{F}_1 + \bar{F}_0 D \bar{F}_1) \\
& + P_{gg}(F_1 \bar{F}_1) \\
& + P_{gr}(F_1 D F_0 + F_1 \bar{D} \bar{F}_1) \\
& + P_{rg}(F_1 \bar{D} \bar{F}_1 + \bar{F}_0 D \bar{F}_1) \\
& + P_{rr}(F_1 \bar{D} F_0 D + \bar{F}_0 D \bar{F}_1 \bar{D} + \bar{F}_0 F_0 D^2 + F_1 \bar{F}_1 \bar{D}^2),
\end{aligned} \tag{D5}$$

$$\begin{aligned}
P_{00} = {} & P_{ll}(F_0^2) \\
& + P_{la}(F_0 \bar{F}_1) \\
& + P_{al}(\bar{F}_1 F_0) \\
& + P_{lg}(F_0 \bar{F}_1) \\
& + P_{gl}(\bar{F}_1 F_0) \\
& + P_{lr}(F_0^2 D + F_0 \bar{F}_1 \bar{D}) \\
& + P_{rl}(F_0^2 D + \bar{F}_1 \bar{D} F_0) \\
& + P_{aa}(\bar{F}_1{}^2) \\
& + P_{ag}(\bar{F}_1{}^2) \\
& + P_{ga}(\bar{F}_1{}^2) \\
& + P_{ar}(\bar{F}_1 F_0 D + \bar{F}_1{}^2 \bar{D}) \\
& + P_{ra}(\bar{F}_1{}^2 \bar{D} + F_0 D \bar{F}_1) \\
& + P_{gg}(\bar{F}_1{}^2) \\
& + P_{gr}(\bar{F}_1 F_0 D + \bar{F}_1{}^2 \bar{D}) \\
& + P_{rg}(\bar{F}_1{}^2 \bar{D} + F_0 D \bar{F}_1) \\
& + P_{rr}(\bar{F}_1{}^2 \bar{D}^2 + F_0 D \bar{F}_1 \bar{D} + F_0^2 D^2 + \bar{F}_1 \bar{D} F_0 D),
\end{aligned} \tag{D6}$$

$$
\begin{aligned}
P_{11} = {} & P_{ll}(\bar{F_0}^2) \\
& + P_{la}(\bar{F_0}F_1) \\
& + P_{al}(F_1\bar{F_0}) \\
& + P_{lg}(\bar{F_0}F_1) \\
& + P_{gl}(F_1\bar{F_0}) \\
& + P_{lr}(\bar{F_0}^2 D + \bar{F_0}F_1\bar{D}) \\
& + P_{rl}(\bar{F_0}^2 D + F_1\bar{D}\bar{F_0}) \\
& + P_{aa}(F_1^2) \\
& + P_{ag}(F_1^2) \\
& + P_{ga}(F_1^2) \\
& + P_{ar}(F_1\bar{F_0}D + F_1^2\bar{D}) \\
& + P_{ra}(F_1^2\bar{D} + \bar{F_0}DF_1) \\
& + P_{gg}(F_1^2) \\
& + P_{gr}(F_1\bar{F_0}D + F_1^2\bar{D}) \\
& + P_{rg}(F_1^2\bar{D} + \bar{F_0}DF_1) \\
& + P_{rr}(F_1^2\bar{D} + \bar{F_0}DF_1\bar{D} + \bar{F_0}^2 D^2\bar{D} + F_1\bar{D}\bar{F_0}D).
\end{aligned}
\tag{D7}
$$

Note that $P_{01} = 1 - P_{10} - P_{00} - P_{11}$. Thus, with the three above equations, we can solve for $P^{'}_{rg}$, $P^{'}_{gr}$, and $P^{'}_{rr}$ in terms of the measured $P_{00}$, $P_{\{10\}}$, $P_{[10]}$ and $P_{11}$, where $P_{\{10\}} = P_{10} + P_{01}$ and $P_{[10]} = P_{10} - P_{01}$. We perform this analysis on the measurements both with the traps off and with the traps on (denoted with a T, as in Table I). These experimentally measured values are shown in Table V, with which we compute the SPAM-corrected values shown in Table I of the main text.

Table V. Experimentally measured (uncorrected) values used to calculate $P^{'}_{rg}$, $P^{'}_{gr}$, and $P^{'}_{rr}$ at both the $\pi$- and $2\pi$-times. The 'T' superscript indicates the values for which the traps were on.

| Variable | Value |
|---|---|
| $P_{\{10\}}(\pi)$ | 0.992(2) |
| $P_{[01]}(\pi)$ | 0.01(1) |
| $P_{00}(\pi)$ | 0.0032(7) |
| $P_{11}(2\pi)$ | 0.992(2) |
| $P_{[01]}(2\pi)$ | 0.004(2) |
| $P_{00}(2\pi)$ | 0.0036(7) |
| $P^T_{\{10\}}(\pi)$ | 0.992(2) |
| $P^T_{[01]}(\pi)$ | 0.004(10) |
| $P^T_{00}(\pi)$ | 0.0032(7) |
| $P^T_{11}(2\pi)$ | 0.987(2) |
| $P^T_{[01]}(2\pi)$ | -0.003(2) |
| $P^T_{00}(2\pi)$ | 0.0030(6) |

## APPENDIX E: Bell state fidelity

### 1. Bounding the Bell state fidelity

Characterizing the state of a quantum system is of fundamental importance in quantum information science. Canonical tomographic methods addressing this task require a measurement of a complete basis set of operators. Such measurements are often expensive or not accessible. More economic approaches can be employed to assess the overlap with a given target state. For example the overlap of a two-qubit state with a Bell state is routinely determined by measuring the populations in the four computational basis states (yielding the diagonal elements of the density operator), in addition with a measurement that probes off-diagonal elements via parity oscillations [8, 60]. To access the latter it is however necessary to perform individual, local operations on the qubits. Here, we present a bound on the Bell state fidelity that can be accessed with only global control and measurements in the computational basis and elaborate on the underlying assumptions.

Specifically, we are interested in the overlap $\mathcal{F}$ of the experimentally created state $\rho$ with a Bell state of the form $|W_\phi\rangle = \frac{1}{\sqrt{2}}(|gr\rangle + e^{i\phi}|rg\rangle)$. This is defined as

$$
\mathcal{F} = \max_{\phi} \langle W_\phi|\rho|W_\phi\rangle = \frac{1}{2}\big(\rho_{gr,gr} + \rho_{rg,rg} + 2|\rho_{gr,rg}|\big). \tag{E1}
$$

Here we denote matrix elements of a density operator $\rho$ in the two-atom atomic basis by $\rho_{i,j} = \langle i|\rho|j\rangle$, with $i, j \in \{gg, gr, rg, rr\}$. Clearly a measurement of $\mathcal{F}$ requires access to the populations in the ground and Rydberg states $\rho_{i,i}$ as well as some of the coherences $\rho_{i,j}$ with $i \neq j$. While the former are direct observables (in particular, we identify $\rho_{i,i}$ with our measured values $P_i$), the latter are not. We can however bound the fidelity $\mathcal{F}$ from below via a bound on $|\rho_{gr,rg}|$. Namely, it can be shown via Cauchy's inequality $|\rho_{a,b}|^2 \leq \rho_{a,a}\rho_{b,b}$ and the normalization of states $\sum_i \rho_{i,i} = 1$ that

$$
|\rho_{gr,rg}|^2 \geq \frac{1}{2}(\mathrm{tr}\left\{\rho^2\right\} - 1) + \rho_{gr,gr}\rho_{rg,rg} \tag{E2}
$$

where $\mathrm{tr}\left\{\rho^2\right\} = \sum_{i,j} |\rho_{i,j}|^2$ is the purity.

Evaluating the bound given by equation Eq. (E2) requires access to the purity (or a lower bound thereof). One can bound the purity from below by the populations in the ground and Rydberg states as

$$
\mathrm{tr}\left\{\rho^2\right\} \geq \sum_i (\rho_{i,i})^2. \tag{E3}
$$

In general Eq. (E3) is a very weak bound. In particular, it does not distinguish between a pure Bell state $|\psi_\phi\rangle$ and the incoherent mixture of the two states $|gr\rangle$ and $|rg\rangle$. However, if the state $\rho$ is close to one of the four atomic basis states (as is the case at the $2\pi$ time of the Rabi evolution), the bound Eq. (E3) becomes tight. This fact allows us to *estimate* the purity of the Bell state in the experiment as follows. The Bell state in our protocol is generated by evolving the state $|gg\rangle$ for a time $T = \pi/\tilde{\Omega}_R$ in the Rydberg-blockade regime. Note that the same evolution should lead to a return to the initial state at time $2T$ in the ideal case. Under the *assumption* that a coupling to the environment decreases the purity of the quantum system (see further exploration of this assumption in the following subsection), we can bound the purity of the state at time $T$ by the purity of the state at time $2T$, which in turn can be bounded by measurements of the atomic populations at time $2T$ via Eq. (E3):

$$\mathrm{tr}\left\{\rho(T)^2\right\} \geq \mathrm{tr}\left\{\rho(2T)^2\right\} \geq \sum_i \rho_{i,i}(2T)^2. \tag{E4}$$

Using this estimated bound on the purity leads to a lower bound on the Bell state fidelity $\mathcal{F}$ at time $T$ solely in terms of the populations in the ground and Rydberg states at times $T$ and $2T$:

$$\begin{aligned}\mathcal{F}(T) \geq \frac{1}{2}\Bigg(&\rho_{gr,gr}(T) + \rho_{rg,rg}(T)\\ &+2\sqrt{\max\left(0, (\textstyle\sum_i \rho_{i,i}(2T)^2 - 1)/2 + \rho_{gr,gr}(T)\rho_{rg,rg}(T)\right)}\Bigg).\end{aligned} \tag{E5}$$

### 2. Bounding an increase in purity due to spontaneous decay

Although we make the assumption that the purity of our state does not increase between times $T$ and $2T$ and assert that this assumption is reasonable, we recognize the hypothetical possibility that dissipative processes such as spontaneous emission can in principle increase the purity of quantum states. We note an increase of purity with time typically occurs only in specially engineered situations (as in optical pumping schemes), and we have no reason to believe such mechanisms are active in our system. In fact, reasonable numerical models of potential decoherence mechanisms are all consistent with a decrease of the purity. Nevertheless, we now analyze how strongly our assumption of purity decrease could potentially be violated given the spontaneous emission rate of our Rydberg state and show that the corresponding decrease of the inferred Bell state fidelity is well within our confidence interval.

We assume that the system can be modeled by a Markovian Master equation of the form:

$$\begin{aligned}\dot{\rho} = \mathcal{L}\rho = -i[H,\rho] &+ \sum_\mu \gamma_\mu (c_\mu \rho c_\mu^\dagger - \frac{1}{2}\{c_\mu^\dagger c_\mu, \rho\})\\ &+ \sum_\mu \bar{\gamma}_\mu (h_\mu \rho h_\mu - \frac{1}{2}\{h_\mu h_\mu, \rho\})\end{aligned} \tag{E6}$$

Here we explicitly distinguish incoherent terms generated by Hermitian jump operators ($h_\mu = h_\mu^\dagger$, e.g. dephasing), and non-Hermitian jump operators ($c_\mu$, e.g. spontaneous emission). We find

$$\frac{d}{dt}\mathrm{tr}\left\{\rho^2\right\} = 2\mathrm{tr}\left\{\rho(\mathcal{L}\rho)\right\} \leq 2\sum_\mu \gamma_\mu \mathrm{tr}\left\{\rho c_\mu \rho c_\mu^\dagger - c_\mu^\dagger c_\mu \rho^2\right\} \tag{E7}$$

which simply reflects the fact that the purity of the quantum state can not increase due to the coherent part of the evolution or due to any incoherent part of the evolution that is generated by Hermitian jump operators (dephasing). Thus the coherent part of the evolution does not affect the bound we obtain in the end. Eq. (E7) can be obtained from Eq. (E6) by noting that $\mathrm{tr}\{\rho[H,\rho])\} = \mathrm{tr}\left\{\rho H \rho - \rho^2 H\right\} = 0$ and $\mathrm{tr}\{\rho[h_\mu,[\rho,h_\mu]]\} = -\mathrm{tr}\{[h_\mu,\rho][\rho,h_\mu]\} = -\mathrm{tr}\left\{([\rho,h_\mu])^\dagger[\rho,h_\mu]\right\} \leq 0$, which gives Eq. (E7).

Now let us assume that the non-Hermitian jump operators correspond to decay from the Rydberg state $|r\rangle$ into some set of states $\{|f\rangle | f = 1, 2, \ldots n\}$ that also include the ground state $|g\rangle \equiv |1\rangle$. The following argument works for arbitrary $n \geq 1$. Since we have two atoms we have $2n$ non-Hermitian jump operators $c_f^{(a)} = |f\rangle_a\langle r|$, where $a = 1, 2$ labels the atoms. With this model we have (denoting the reduced state of atom $a$ by $\rho^{(a)}$):

$$\begin{aligned}\frac{d}{dt}\mathrm{tr}\left\{\rho^2\right\} &\leq 2\sum_{f,a}\Gamma_f \mathrm{tr}\left\{\rho c_f^{(a)} \rho c_f^{(a)\dagger} - c_f^{(a)\dagger} c_f^{(a)} \rho^2\right\}\\ &= 2\sum_{f,a}\Gamma_f(\rho_{f,f}^{(a)}\rho_{r,r}^{(a)} - \rho_{r,r}^{(a)}\rho_{r,r}^{(a)} - \sum_{e\neq r}\rho_{r,e}^{(a)}\rho_{e,r}^{(a)})\\ &\leq 2\sum_{f,a}\Gamma_f(\rho_{f,f}^{(a)}\rho_{r,r}^{(a)} - \rho_{r,r}^{(a)}\rho_{r,r}^{(a)})\end{aligned} \tag{E8}$$

where $\Gamma_F$ is the single-atom decay rate from $|r\rangle$ to $|f\rangle$. Note that $\rho_{f,f}^{(a)}\rho_{r,r}^{(a)} - \rho_{r,r}^{(a)}\rho_{r,r}^{(a)} \leq (1-\rho_{r,r}^{(a)})\rho_{r,r}^{(a)} - \rho_{r,r}^{(a)}\rho_{r,r}^{(a)} \leq 1/8$. This gives the final result

$$\frac{d}{dt}\mathrm{tr}\left\{\rho^2\right\} \leq \frac{1}{2}\sum_f \Gamma_f = \frac{1}{2}\Gamma \tag{E9}$$

That is, the rate at which the purity increases is upper bounded by half the rate at which a single atom in the Rydberg state decays into other states by spontaneous emission. Over a time interval of length $T$ the 2-atom purity can thus not increase by more than $T\Gamma/2$.

Using our blockaded $\pi$-time for $T$ and Rydberg state decay rate for $\Gamma$, we evaluate this bound on the purity increase to be $3.2 \times 10^{-4}$. This would lead to a decrease in our bound on the Bell state fidelity by $1.6 \times 10^{-4}$ for both the cases of tweezers off and tweezers on, which is significantly smaller than our quoted error for these values.

## APPENDIX F: Rydberg laser system

The Rydberg laser system is based on a Toptica laser, in which an extended cavity diode laser (ECDL) at $\lambda_{\mathrm{IR}} = 1266.8$ nm seeds a tapered amplifier (TA) with output power up to $\approx 2$ W, which is then frequency doubled via second harmonic generation (SHG) in a bowtie cavity to obtain up to $\approx 1$ W at $\lambda_{\mathrm{Red}} = 633.4$ nm, which is then frequency doubled in a second bowtie cavity to obtain fourth harmonic generation (FHG) with up to $\approx 0.4$ W at $\lambda_{\mathrm{UV}} = 316.7$ nm. The fundamental laser at $\lambda_{\mathrm{IR}} = 1266.8$ nm is stabilized to an ultralow expansion (ULE) cavity system (Stable Laser Systems) of length 10 cm with finesse of $\approx 14000$ and line width (full width at half maximum) of $\approx 110$ kHz. The finesse was measured by performing cavity ringdown spectroscopy [61]. We currently do not filter the fundamental laser with the cavity [8], but we are prepared to implement this approach. Further discussion on the laser frequency stability can be found in Appendix G.

We use a beam power of $P_R = 28.1(4)$ mW, measured immediately before it enters the vacuum cell (through 4 mm of uncoated quartz). The geometric mean $1/e^2$ waist radius of the beam at the position of the atoms is $\overline{w}_0^R = 18(1)$ $\mu$m. These conditions correspond to the Rabi frequency used throughout the text of $\Omega_R \approx 2\pi \times 6 - 7$ MHz. The maximum power we can achieve is $\approx 110$ mW, for which we observe a Rabi frequency of $\approx 13$ MHz. The Rydberg pulses are derived from an AOM, which limits the rise and fall time to $\approx 40$ ns – corresponding to the $\pi$-pulse time for $\Omega_R \approx 2\pi \times 13$ MHz. We observe an asymmetric reduction in Rabi signal contrast by $\approx 1 - 2\%$ at the multiples of $2\pi$, unlike conventional detuned Rabi oscillations where the contrast reduction occurs at the odd multiples of $\pi$, which we attribute to early-time dynamics during the AOM switching. We do not use an optical fiber, so there is limited spatial – and thus spectral – filtering between the AOM and the atoms. Accordingly, we intentionally work with $\Omega_R \approx 2\pi \times 6 - 7$ MHz such that the $\pi$-pulse time is sufficiently slow compared to the AOM rise and fall times. However, when operating at $\Omega_R \approx 2\pi \times 13$ MHz we observe long-time coherence similar to, or slightly better than, the reported values in the main text for $\Omega_R \approx 2\pi \times 6 - 7$ MHz. Measured results under all conditions are consistent with the numerical analysis summarized in Fig. 6 below.

## APPENDIX G: Rydberg decoherence mechanisms

For a non-interacting case where Rydberg atoms in a tweezer array are well separated, the Hamiltonian $H$ driving Rabi oscillations is

$$H = \sum_{i=1}^{N} \Omega_{R,i} S_i^x + \Delta_i S_i^z, \tag{G1}$$

where $\Omega_{R,i}$ and $\Delta_i$ are the Rabi frequency and the detuning for the atom at site $i$, $S^\mu$ are the spin-1/2 operators with $\mu = x, y, z$, and $N$ is the total number of atoms. Variations in the Rabi frequency and detuning, manifesting either as non-uniformity across the tweezer array (e.g. from non-uniform beam alignment) or as random noise, lead to a decay in the array-averaged Rabi signal. In our system, we measure a $1/e$ decay time of $\approx$7 $\mu s$ at a Rabi frequency of 6 MHz [see Fig. 3(a) of the main text]. In this section, we present a model of decoherence mechanisms that accounts for our observed decay.

As a preliminary, we begin by confirming that the spatial variation of Rabi frequency across different tweezers is less than 0.2%, and that no variation of detuning across the array is observed. We conclude that non-uniformity is not a dominant contributor to our observed Rabi decay.

Therefore, we focus here on three factors that induce random noise in the Rabi frequency and detuning: atomic motion, laser phase noise, and laser intensity noise. We perform Monte Carlo-based simulations [17] that take into account these noise sources as well as the finite lifetime $\approx$80 $\mu$s of the $n = 61$ Rydberg state due to spontaneous emission. In the following subsections, we discuss relative contributions from these noise sources.

### 1. Atomic motion

An atom with a nonzero momentum shows a Doppler shift relative to the bare resonance frequency. At the beginning of Rabi interrogation, the momentum distribution, and thus the distribution of Doppler shifts, follows that of an atom in a trap. More specifically, for an atom at temperature $T$ trapped in a harmonic potential with the radial trap frequency $\omega_r$, the Doppler shift distribution can be modeled as a normal distribution with the standard deviation $\Delta_T$:

$$\Delta_T = \frac{k_L}{m} \sqrt{\frac{\hbar m \omega_r}{2 \tanh(\hbar\omega_r / 2k_B T)}}, \tag{G2}$$

where $m$ is the mass of $^{88}$Sr and $k_L$ is the wavevector of the Rydberg excitation light.

The radial temperature of our atomic array (along the axis of propagation of the Rydberg beam) is measured via sideband spectroscopy on the clock transition [34] to be $T_r \approx 2.5$ $\mu$K at a radial trap frequency of $\omega_r \approx 2\pi \times 78$ kHz. We adiabatically ramp down the trap by a factor of 10 before Rydberg interrogation, thereby reducing the temperature and the trap frequency by a factor of $\sqrt{10}$ (which we also confirm via further sideband spectroscopy). Using Eq. G2, we estimate the Doppler broadening to be $\Delta_T \approx 2\pi \times 30$ kHz. At a Rabi frequency of $\Omega_R \approx 2\pi \times 6$ MHz, the expected Doppler decoherence timescale is $\tau \sim \Omega_R/\Delta_T^2 \approx$10 ms, which is three orders of magnitudes longer than the measured value $\approx$7 $\mu$s. This implies that motional effects are negligible in the Rabi decoherence dynamics.

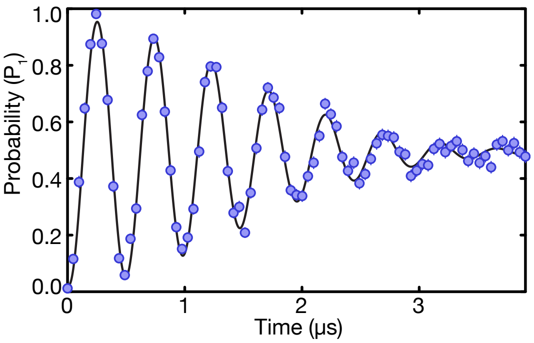

FIG. 5. Ramsey interferometry. We use a detuning of 2 MHz between the two pulses to show oscillations with a characteristic $1/e$ decay time $\tau_{\text{Ramsey}} \approx 2$ $\mu$s. A sine-modulated Gaussian decay is used for the fit (solid line).

### 2. Laser phase noise

Phase noise manifests as random temporal fluctuation of the detuning $\Delta$ in the Hamiltonian in Eq. G1. Since the frequency of the Rydberg laser is stabilized to a ULE reference cavity via the Pound-Drever-Hall (PDH) method, we use an in-loop PDH error signal derived from the cavity reflection to extract a phase noise spectrum (see Ref. [17] for the detailed procedures of phase noise extraction). The obtained noise power spectral density, predicting a RMS frequency deviation of ≈0.6 MHz after fourth-harmonic generation, allows us to generate random time-varying detuning profiles that are fed into our Monte Carlo simulations to extract a predicted decay time. Note that while the estimated laser linewidth is $\sim 1-10$ kHz, phase noise from the servo bumps centered at $\nu_{\text{SB}} \approx 0.6$ MHz is highly relevant since $\Omega_R > \nu_{\text{SB}}$, and in fact dominates the RMS.

Since the cavity filters phase noise beyond its linewidth, this noise is suppressed on the measured PDH signal as compared to the actual noise of the laser light that we use for Rydberg interrogation. We therefore correct our measured phase noise spectrum with a cavity roll-off factor [62] obtained from the cavity linewidth and finesse, which results in an increase in noise as compared to the uncorrected measured spectrum. However, we can also use the uncorrected spectrum to predict the phase noise we would have if we used the filtered cavity light to generate our Rydberg light via a technique described in Ref. [8]. The results in Fig. 6 show simulated results both with and without cavity filtering.

Our simulations (without cavity filtering, as in our current setup) predict a Ramsey decay time of $\approx 2$ $\mu s$ with a Gaussian envelope, which is consistent with our experimental observation. In principle, Doppler broadening $\Delta_T$ could also lead to dephasing in Ramsey signals; however, the corresponding $1/e$ decay time is expected to be $\tau_{\text{Ramsey}} = \sqrt{2}/\Delta_T = 7.5$ $\mu s$, longer than the observed 2 $\mu$s, suggesting that laser phase noise is dominant over motional effects in our Ramsey signal.

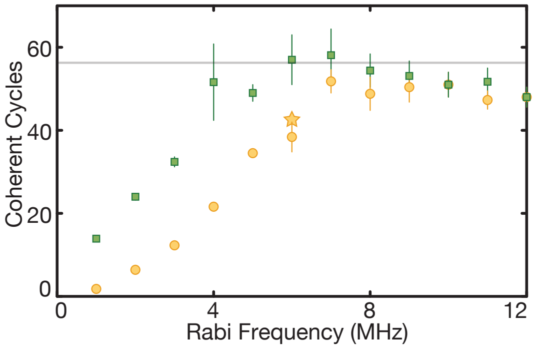

FIG. 6. Simulated and measured $1/e$ coherence vs Rabi frequency. The star represents the measured data shown in Fig. 3(a), and the circle and square points represent numerical modeling with measured laser phase and intensity noise profiles. The yellow circles show the case when cavity phase noise filtering is *not* performed (as in this work), and the green squares show the case where cavity phase noise filtering *is* performed. The horizontal gray line shows the upper limit due to measured intensity noise fluctuations with RMS deviation of 0.8% (see Eq. (G3)).

### 3. Laser intensity noise

Our intensity noise predominantly originates directly from the Rydberg laser. This intensity noise is composed of both high-frequency fluctuations compared to the pulse length, and lower frequency (effectively shot-to-shot) fluctuations. Using a UV avalanche photodetector (APD130A2, Thorlabs), we measure that the intensity noise fluctuations between different experimental trials exhibit an expected scaling of $\sigma_{\text{RMS}} \sim 1/\sqrt{L}$, where $L$ is the pulse duration, saturating to 0.8% when $L > 1$ $\mu$s. Note that the pulses are too fast to stabilize with an AOM during interrogation, and that we employ a sample-and-hold method.

In the presence of only intensity noise following a normal distribution with standard deviation $\sigma_{\text{RMS}}$, one can derive an analytical expression for a $1/e$ Rabi decay time as $\tau_{\text{Rabi}} = 2\sqrt{2}/(\Omega_R \sigma_{\text{RMS}})$ where $\Omega_R$ is the nominal, noise-free Rabi frequency. In the intensity noise limited regime, we thus expect a Rabi lifetime $\mathcal{N}_{\text{Rabi}}$ (in oscillation cycles) to be Rabi frequency-independent (see the line in Fig. 6):

$$\mathcal{N}_{\text{Rabi}} = \frac{\Omega_R \tau_{\text{Rabi}}}{2\pi} = \frac{\sqrt{2}}{\pi \sigma_{\text{RMS}}}. \tag{G3}$$

### 4. Summary

Including all the discussed noise sources (atomic motions, phase noise, intensity noise) as well the finite state lifetime and a Rydberg probe-induced light shift (discussed in a subsequent section), we calculate $\mathcal{N}_{\text{Rabi}}$ as a function of drive frequency, as shown in Fig. 6. We find that the simulated Rabi oscillation agrees well with

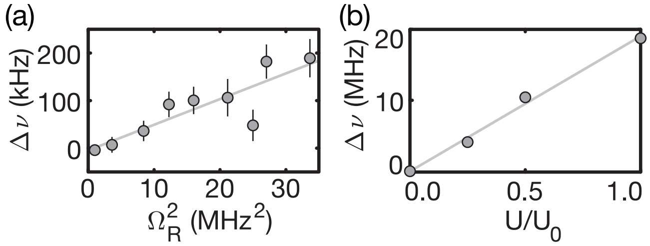

FIG. 7. Light shifts of $|r\rangle$ from the Rydberg laser and the tweezer light. (a) The differential shift of the $|g\rangle \leftrightarrow |r\rangle$ resonance between $\Omega_R^{\text{init}} = 2\pi \times 1$ MHz and variable $\Omega_R$ versus $\Omega_R^2$. This set of data was measured with the two-rail self-comparison technique utilized in Ref. [34]. The fit line reflects the quadratic scaling $\Delta\nu = \kappa^{\text{UV}}_{|r\rangle}\Omega_R^2$, with $\kappa^{\text{UV}}_{|r\rangle} = 5.1(7)$ kHz/MHz$^2$. (b) The differential shift of the $|g\rangle \leftrightarrow |r\rangle$ resonance between the dark case $\text{U} = 0$ where the tweezers are extinguished during excitation, and the bright case with variable $|g\rangle$-state depth U up to $\text{U}_0 \approx k_\text{B} \times 450$ $\mu$K $\approx h \times 9.4$ MHz. This fit shows a linear dependence with $\Delta\nu = \kappa^{\text{T}}_{|r\rangle}\text{U}$, where $\kappa^{\text{T}}_{|r\rangle} = 18.8(9)$ MHz/U$_0$.

the experimental result at a Rabi frequency of 6 MHz. While the Rabi lifetime improves with increasing Rabi frequency, it becomes saturated to $\mathcal{N}_{\text{Rabi}} \approx 56$ at high Rabi frequencies due to intensity noise fluctuations. Interestingly, we note that there is a crossover between a phase noise-limited regime at low Rabi frequencies and an intensity noise-limited regime at higher Rabi frequencies, which for our phase and intensity noise profiles occurs at $\Omega_R \approx 2\pi \times 7$ MHz. Our numerical simulations suggest that, at Rabi frequencies less than this value, cavity phase noise filtering [8] can enhance the long-time Rabi coherence.

## APPENDIX H: Rydberg state systematics

### 1. State identification and quantum defects

The Rydberg state $|r\rangle$ we use for this work is the 5s61s $^3\text{S}_1$ $m_J = 0$ state of $^{88}$Sr. To confirm the quantum numbers, we measure the transition wavelengths of $n = 48, 49, 50, 61$ for the $^3\text{S}_1$ series and of $n = 47, 48, 49$ for the $^3\text{D}_1$ series and find nearly perfect agreement with the values predicted by the quantum defects given in Ref. [42].

### 2. Rydberg probe-induced light shift

The pulse generation for our Rydberg interrogation is facilitated by switching on and off an acousto-optic modulator (AOM). However, due to the finite speed of sound in the AOM crystal, the switch-on and switch-off times are limited to tens of nanoseconds. This timescale begins to approach the timescale of our $\pi$-pulses for Rabi frequencies greater than ≈10 MHz. This poses a potential problem if there is also a significant intensity-dependent light shift of the resonance frequency due to the Rydberg interrogation beam. For example, a detuning that changes significantly on the timescale of the Rabi frequency could lead to non-trivial dynamics on the Bloch sphere, causing unfaithful execution of Rabi oscillations. We note that such an effect scales unfavorably with increasing Rabi frequency, as both the relevant timescale becomes shorter and the magnitude of the shift becomes quadratically larger.

To this end, we operate at Rabi frequencies smaller than 6 MHz to isolate the pure Rydberg laser-induced light shift from the undesired AOM-related transient effect. Using the two-rail clock operation technique described in Ref. [34], we measure the light shift induced by the Rydberg beam and find it to be described by $\Delta\nu = \kappa^{\text{UV}}_{|r\rangle}\Omega_R^2$ with $\kappa^{\text{UV}}_{|r\rangle} = 5.1(7)$ kHz/MHz$^2$, as shown in Fig. 7(a).

### 3. Tweezer-induced light shift

We have demonstrated high-fidelity blockaded Rabi oscillations *without* extinguishing the tweezer traps. To gain a partial understanding of this observation, we measure the light shift of $|r\rangle$ in the tweezers with wavelength $\lambda_\text{T} = 813.4$ nm and waist of $w_\text{T} \approx 800$ nm. We measure the differential shift of the $|g\rangle \leftrightarrow |r\rangle$ resonance between the dark case $\text{U} = 0$ where the tweezers are extinguished during excitation, and the bright case with variable $|g\rangle$-state depth U up to $\text{U}_0 \approx 450$ $\mu$K $\approx h \times 9.4$ MHz. This fit shows a linear dependence with $\Delta\nu = \kappa^{\text{T}}_{|r\rangle}\text{U}$, where $\kappa^{\text{T}}_{|r\rangle} = 18.8(9)$ MHz/U$_0$. We conclude that $\kappa^{\text{T}}_{|r\rangle} \approx -\kappa^{\text{T}}_{|g\rangle}$ at this tweezer wavelength and waist. We leave the detailed modeling of the polarizability to future work.

### 4. Diamagnetic shift from magnetic fields

We measure a magnetic-field-dependent shift of the Rydberg resonance that is quadratic in the magnitude of the field. We attribute this shift to the diamagnetic effect, which has a Hamiltonian given by $H_{dm} = \frac{1}{8m_e}|\boldsymbol{d} \times \boldsymbol{B}|^2$ [63], where $\boldsymbol{d}$ is the dipole operator, $\boldsymbol{B}$ is the magnetic field, and $m_e$ is the electron mass. This Hamiltonian gives rise to a first order shift in the energy that is quadratic in the magnitude of the field such that $\Delta\nu_{dm} = \beta|\boldsymbol{B}|^2$, where $\beta$ is a state dependent quantity that increases with the principal quantum number $n$. For 5s61s $^3\text{S}_1$ $m_J = 0$, we experimentally measure $\beta \approx 3.4$ kHz/G$^2$.

We compare this value to a value predicted by performing exact diagonalization of $H_{dm}$ on a limited manifold of Rydberg states in a similar fashion to Ref. [63] while using quantum defects from Ref. [42]. This numerical procedure produces $\beta_{\text{predicted}} = 2.9$ kHz/G$^2$ for our state, in near agreement with our measured value.

[1] M. Saffman, T. G. Walker, and K. Mølmer, Reviews of Modern Physics **82**, 2313 (2010).
[2] P. Schauß *et al.*, Science **347**, 1455 (2015).
[3] H. Labuhn *et al.*, Nature **534**, 667 (2016).
[4] H. Bernien *et al.*, Nature **551**, 579 (2017).
[5] A. Browaeys, D. Barredo, and T. Lahaye, Journal of Physics B: Atomic, Molecular and Optical Physics **49**, 152001 (2016).
[6] M. Saffman, Journal of Physics B: Atomic, Molecular and Optical Physics **49**, 202001 (2016).
[7] Y.-Y. Jau, A. M. Hankin, T. Keating, I. H. Deutsch, and G. W. Biedermann, Nature Physics **12**, 71 (2016).
[8] H. Levine *et al.*, Physical Review Letters **121**, 123603 (2018).
[9] T. M. Graham *et al.*, Physical Review Letters **123**, 230501 (2019).
[10] H. Levine *et al.*, Physical Review Letters **123**, 170503 (2019).
[11] A. Omran *et al.*, Science **365**, 570 (2019).
[12] T. Monz *et al.*, Physical Review Letters **106**, 130506 (2011).
[13] C. Song *et al.*, Science **365**, 574 (2019).
[14] D. Barredo, S. de Leseleuc, V. Lienhard, T. Lahaye, and A. Browaeys, Science **354**, 1021 (2016).
[15] M. Endres *et al.*, Science **354**, 1024 (2016).
[16] A. Kumar, T.-Y. Wu, F. Giraldo, and D. S. Weiss, Nature **561**, 83 (2018).
[17] S. de Léséleuc, D. Barredo, V. Lienhard, A. Browaeys, and T. Lahaye, Physical Review A **97**, 053803 (2018).
[18] S. Mauger, J. Millen, and M. P. A. Jones, Journal of Physics B: Atomic, Molecular and Optical Physics **40**, F319 (2007).
[19] B. J. DeSalvo *et al.*, Physical Review A **93**, 022709 (2016).
[20] C. Gaul *et al.*, Physical Review Letters **116**, 243001 (2016).
[21] F. Camargo *et al.*, Physical Review Letters **120**, 083401 (2018).
[22] M. A. Norcia, A. W. Young, and A. M. Kaufman, Physical Review X **8**, 041054 (2018).
[23] A. Cooper *et al.*, Physical Review X **8**, 041055 (2018).
[24] S. Saskin, J. T. Wilson, B. Grinkemeyer, and J. D. Thompson, Physical Review Letters **122**, 143002 (2019).
[25] A. D. Ludlow, M. M. Boyd, J. Ye, E. Peik, and P. O. Schmidt, Reviews of Modern Physics **87**, 637 (2015).
[26] L. I. R. Gil, R. Mukherjee, E. M. Bridge, M. P. A. Jones, and T. Pohl, Physical Review Letters **112**, 103601 (2014).
[27] E. M. Kessler *et al.*, Physical Review Letters **112**, 190403 (2014).
[28] R. Kaubruegger *et al.*, arXiv:1908.08343 (2019).
[29] P. Kómár *et al.*, Nature Physics **10**, 582 (2014).
[30] A. J. Daley, M. M. Boyd, J. Ye, and P. Zoller, Physical Review Letters **101**, 170504 (2008).
[31] A. V. Gorshkov *et al.*, Physical Review Letters **102**, 110503 (2009).
[32] A. J. Daley, Quantum Information Processing **10**, 865 (2011).
[33] J. P. Covey, I. S. Madjarov, A. Cooper, and M. Endres, Physical Review Letters **122**, 173201 (2019).
[34] I. S. Madjarov *et al.*, Physical Review X **9**, 041052 (2019).
[35] See Supplemental Material .
[36] M. A. Norcia *et al.*, Science **366**, 93 (2019).
[37] W. E. Cooke, T. F. Gallagher, S. A. Edelstein, and R. M. Hill, Physical Review Letters **40**, 178 (1978).
[38] G. Lochead, D. Boddy, D. P. Sadler, C. S. Adams, and M. P. A. Jones, Physical Review A **87**, 053409 (2013).
[39] H. Pichler, S.-T. Wang, L. Zhou, S. Choi, and M. D. Lukin, arXiv:1808.10816 (2018).
[40] V. Lienhard *et al.*, Physical Review X **8**, 021070 (2018).
[41] E. Guardado-Sanchez *et al.*, Physical Review X **8**, 021069 (2018).
[42] C. L. Vaillant, M. P. A. Jones, and R. M. Potvliege, Journal of Physics B: Atomic, Molecular and Optical Physics **45**, 135004 (2012).
[43] D. Barredo *et al.*, arXiv:1908.00853 (2019).
[44] R. Mukherjee, J. Millen, R. Nath, M. P. A. Jones, and T. Pohl, Journal of Physics B: Atomic, Molecular and Optical Physics **44**, 184010 (2011).
[45] E. Knill, Nature **434**, 39 (2005).
[46] F. Arute *et al.*, Nature **574**, 505 (2019).
[47] L. Karpa, A. Bylinskii, D. Gangloff, M. Cetina, and V. Vuletić, Physical Review Letters **111**, 163002 (2013).
[48] T. Huber, A. Lambrecht, J. Schmidt, L. Karpa, and T. Schaetz, Nature Communications **5**, 5587 (2014).
[49] D. Barredo, V. Lienhard, S. de Léséleuc, T. Lahaye, and A. Browaeys, Nature **561**, 79 (2018).
[50] J. I. Cirac and P. Zoller, Nature **404**, 579 (2000).
[51] F. Engel *et al.*, Physical Review Letters **121**, 193401 (2018).
[52] R. Mukherjee, Physical Review A **100**, 013403 (2019).
[53] T. K. Langin, G. M. Gorman, and T. C. Killian, Science **363**, 61 (2019).
[54] J. Wilson *et al.*, arXiv:1912.08754 (2019).
[55] A. Taichenachev *et al.*, Physical Review Letters **96**, 083001 (2006).
[56] Z. Barber *et al.*, Physical Review Letters **96**, 083002 (2006).
[57] Y. Wang, A. Kumar, T.-Y. Wu, and D. S. Weiss, Science **352**, 1562 (2016).
[58] W. M. Itano, D. J. Heinzen, J. J. Bollinger, and D. J. Wineland, Physical Review A **41**, 2295 (1990).
[59] B. Zhu *et al.*, Physical Review Letters **112**, 070404 (2014).
[60] D. Leibfried *et al.*, Nature **438**, 639 (2005).
[61] D. Z. Anderson, J. C. Frisch, and C. S. Masser, Applied Optics **23**, 1238 (1984).
[62] W. Nagourney, *Quantum Electronics for Atomic Physics and Telecommunication*, 2 ed. (OUP Oxford, 2014).
[63] S. Weber *et al.*, Journal of Physics B: Atomic, Molecular and Optical Physics **50**, 133001 (2017).